



# $\beta$ -Bi<sub>2</sub>O<sub>3</sub> and Er<sup>3+</sup> doped $\beta$ -Bi<sub>2</sub>O<sub>3</sub> single crystalline nanosheets with exposed reactive {0 0 1} facets and enhanced photocatalytic performance

Hang Liu<sup>a</sup>, Man Luo<sup>a</sup>, Juncheng Hu<sup>a,\*</sup>, Tengfei Zhou<sup>a,b</sup>, Rong Chen<sup>c</sup>, Jinlin Li<sup>a</sup>

<sup>a</sup> Key Laboratory of Catalysis and Materials Science of the State Ethnic Affairs Commission & Ministry of Education, South-Central University for Nationalities, Wuhan 430074, PR China

<sup>b</sup> Australian Institute for Innovative Materials, University of Wollongong, NSW 2522, Australia

<sup>c</sup> Key Laboratory for Green Chemical Process of Ministry of Education, Hubei Key Laboratory of Novel Reactor & Green Chemical Technology, Wuhan Institute of Technology, Xiongchu Avenue, Wuhan 430073, PR China



## ARTICLE INFO

### Article history:

Received 19 January 2013

Received in revised form 28 March 2013

Accepted 1 April 2013

Available online 8 April 2013

### Keywords:

Upconversion

$\beta$ -Bi<sub>2</sub>O<sub>3</sub>

Nanosheets

Facets

Photocatalysis

## ABSTRACT

Upconverter Er<sup>3+</sup> doped  $\beta$ -Bi<sub>2</sub>O<sub>3</sub> nanosheets with selectively exposed reactive {0 0 1} facets as the main external surfaces were fabricated by a novel and simple approach for the first time. The products were characterized by X-ray powder diffraction, transmission electron microscopy, high-resolution transmission electron microscopy and UV-vis diffuse reflectance spectroscopy. The introduction of 0.8 wt% Er<sup>3+</sup> significantly improved the photocatalytic activities of the  $\beta$ -Bi<sub>2</sub>O<sub>3</sub>. The enhanced photocatalytic activity of  $\beta$ -Bi<sub>2</sub>O<sub>3</sub> nanosheets can be attributed to the exposed reactive {0 0 1} facets and the dopant Er<sup>3+</sup> which can transform visible light into ultraviolet light. Both the acetic acid and alcohol contributed to the formation of nanosheets. This synthetic approach exhibited good versatility in fabricating other porous materials.

© 2013 Elsevier B.V. All rights reserved.

## 1. Introduction

Micro/nanostructure semiconductor materials with different morphologies exhibit diverse physicochemical properties and lead to very different catalytic activity [1,2]. Two dimensional (2D) structural semiconductor materials like nanosheet, plate, disk or film attract increasing interests due to their high percentage of selectively exposed reactive facets and fast separation of electron and hole [3–6]. Different exposed crystalline facets may have very different catalytic activity, such as the {0 0 1} and the {1 0 1} surfaces of TiO<sub>2</sub>, the {0 0 1} and {0 1 0} facets of BiOCl and the {1 1 0} and {1 0 0} facets of Ag<sub>3</sub>PO<sub>4</sub> [7–10]. Especially, the porous single crystalline nanosheets that possess considerable potential in the frontiers of environment and energy due to their exposed highly reactive surfaces, and free of grain boundaries which could provide large amount of reaction sites and enable rapid charges generation and transport, while all of which are very important for catalysis and energy conversion. For example, porous ZnO nanosheets become a hot topic, nanoporous palladium, porous single crystal Te plates are also reported [11,12]. The fabrication of porous materials

generally relies on template, etching or ion exchange methods, all of which required sacrificial materials as templates. Template-free approaches offer apparent advantages in avoiding the limitation of template structures and the interference of template agents. However, the preparations of porous single crystalline nanosheets with exposed reactive facet by a general template-free method are scarcely reported.

Bismuth trioxide, known for the polymorphic feature including stable  $\alpha$ ,  $\gamma$  phase and metastable  $\beta$ ,  $\delta$  phase, high refractive index, dielectric permittivity, as well as good photoelectrical conductivity and thermal properties, is widely used in various applications. As a p-type semiconductor, Bi<sub>2</sub>O<sub>3</sub> is an active photocatalyst and attracts many interests owing to its strong oxidizing ability that can oxidize water via direct generation of  $\cdot$ O<sub>2</sub><sup>–</sup> and  $\cdot$ OH. Among the four crystal phases,  $\beta$ -Bi<sub>2</sub>O<sub>3</sub> has the narrowest band gap ( $E_g \approx 2.6$  eV) which makes it have a broad light absorption range. While studies on Bi<sub>2</sub>O<sub>3</sub> were focused mainly on its composites such as BiOBr, Bi<sub>2</sub>WO<sub>6</sub>, Bi<sub>2</sub>TiO<sub>5</sub> and BiVO<sub>4</sub>, etc., single crystalline Bi<sub>2</sub>O<sub>3</sub> as photocatalyst attracted few reports [13–16]. Besides, the reported Bi<sub>2</sub>O<sub>3</sub> morphology includes nanowires/nanofibers, ultrathin films, quantum dots and 3D spheres, sheet-like single crystalline Bi<sub>2</sub>O<sub>3</sub> with regular quadrate holes and exposed reactive {0 0 1} facets has not been reported [17–20]. Brezesinski and his coworkers recently reported a  $\beta$ -Bi<sub>2</sub>O<sub>3</sub> mesoporous film, but the requirement

\* Corresponding author. Tel.: +86 27 67841302; fax: +86 27 67841302.

E-mail address: [junchenghuhu@hotmail.com](mailto:junchenghuhu@hotmail.com) (J. Hu).

of complex copolymer in its preparation, relatively high treatment temperature and poor photocatalysis activity impede the application of  $\beta$ - $\text{Bi}_2\text{O}_3$  mesoporous film [21].

Here, for the first time, porous single crystalline  $\beta$ - $\text{Bi}_2\text{O}_3$  nanosheet with exposed  $\{0\ 0\ 1\}$  crystal facets was successfully synthesized using a simple template-free method. It was proposed that the formation of the square holes on  $\text{Bi}_2\text{O}_3$  sheets was attributed to a higher removal rate of defects on the  $\text{Bi}_2\text{O}_3$  precursor than crystallization rate during calcination. The surface energies of the  $\beta$ - $\text{Bi}_2\text{O}_3$  facets were studied through the DFT, and  $\{0\ 0\ 1\}$  facets were proved to exhibit higher surface energy than  $\{1\ 1\ 0\}$  and  $\{1\ 0\ 0\}$  facets. By introducing upconversion (UC) element erbium and varying the doping dosage of  $\text{Er}^{3+}$ , the porous  $\text{Bi}_2\text{O}_3$  nanosheets exhibited an enhanced photoactivity. The enhanced photocatalytic activity of  $\beta$ - $\text{Bi}_2\text{O}_3$  nanosheets can be attributed to the exposed reactive  $\{0\ 0\ 1\}$  facets and the dopant  $\text{Er}^{3+}$  which can transform visible light into ultraviolet light. Besides, the synthetic method shows a good universality in the synthesis of porous erbium oxide and nickel oxide and may be extended to the synthesis of other materials.

## 2. Experimental

### 2.1. Preparation of porous $\beta$ - $\text{Bi}_2\text{O}_3$ nanosheets

All of the chemicals were purchased from Sinopharm Chemical Reagent Co., Ltd. (Shanghai, China), analytical grade, and used as received without any further treatment. In this reaction acetic acid is solvent, and ethanol is used as diluent. 8 mmol  $\text{Bi}(\text{NO}_3)_3 \cdot 6\text{H}_2\text{O}$  was first dissolved in 10 mL acetic acid, after complete dissolution, 70 mL ethanol was added under vigorous stirring. The resultant clear solution was then transferred to a 100 mL Teflon-lined stainless steel autoclave, followed by heating and maintaining at 180 °C for 20 h. Subsequently, the autoclave was cooled to room temperature. The solution was filtered and the filtered material was washed with deionized water and ethanol for several times. After drying at 60 °C for 6 h, a gray  $\text{Bi}_2\text{O}_3$  precursor powder was collected and then calcined at 300 or 400 °C for 4 h at a rate of 5 °C/min. The final yellow powder was the porous single crystalline  $\beta$ - $\text{Bi}_2\text{O}_3$ . Replacing ethanol with equal amount of n-hexanol or n-hexane, porous  $\beta$ - $\text{Bi}_2\text{O}_3$  can also be successfully fabricated.

### 2.2. Preparation of porous $\text{Er}^{3+}$ -doped $\text{Bi}_2\text{O}_3$

The process is identical with the preparation of undoped  $\beta$ - $\text{Bi}_2\text{O}_3$  single crystalline, just added a certain amount of  $\text{Er}(\text{NO}_3)_3 \cdot 6\text{H}_2\text{O}$  dissolved in ethanol into the reaction solution before heating.

### 2.3. Preparation of porous $\text{Er}_2\text{O}_3$ and $\text{NiO}$ nanostructure

A similar approach was employed to synthesize  $\text{Er}_2\text{O}_3$  and  $\text{NiO}$ . In this reaction acetic acid was employed as solvent, ethanol was diluent. 8 mmol  $\text{Er}(\text{NO}_3)_3 \cdot 6\text{H}_2\text{O}$  or  $\text{Ni}(\text{NO}_3)_2 \cdot 6\text{H}_2\text{O}$  was first dissolved in 10 mL acetic acid, after completely dissolved, 70 mL ethanol was added to above solution under vigorous stirring. The solution was then transferred to a 100 mL Teflon-lined stainless steel autoclave and following heated and maintained at 180 °C for 12 h. Subsequently, the autoclave was cooled to room temperature. The solution was filtered and the filtered material was washed with deionized water and ethanol for several times. After dried at 60 °C for 6 h a pink  $\text{Er}_2\text{O}_3$  or green  $\text{NiO}$  precursor powder was acquired and then calcined the precursor at 500 °C for 4 h at a rate of 5 °C/min, the final powder was the porous  $\text{Er}_2\text{O}_3$  or  $\text{NiO}$  samples.

### 2.4. Photocatalytic activities measurements

The photocatalytic activities were evaluated by the degradation of RhB under simulated sunlight irradiation using a 350 W Xe lamp. Firstly, 50 mg catalysts were dispersed in 50 mL  $1 \times 10^{-5}$  mol/L RhB by ultrasound and then stirred in the dark for 5 h to reach the adsorption desorption equilibrium. At given time intervals, 3 mL liquid were sampled and filtered to remove the catalyst particles before the UV-vis spectrophotometer analysis.

### 2.5. Characterizations

The TEM images were taken on a Tecnai G20 (FEI Co., Holland) microscope using an accelerating voltage of 200 KV. The HRTEM images were taken on a Tecnai G20 (FEI Co., Holland) microscope operating at 300 kV. The XRD patterns were characterized by a Bruker D8 Advance powder X-ray diffraction (XRD) using monochromatized  $\text{Cu K}\alpha$  radiation. The FTIR spectra were recorded on a Nicolet NEXUS 470 FTIR ESR using KBr as background. The UV-vis DRS were collected on a Shimadzu UV-2550 spectrophotometer from 200 to 800 nm using  $\text{BaSO}_4$  as background. The UV-vis spectra of RhB were analyzed using a Shimadzu UV-2550 spectrophotometer. The total organic carbon (TOC) content of the RhB solution after degradation test was detected by a Multi N/C 3100 Analyser (Analytic Jena, Germany).

### 2.6. Computational details

Our surface energy calculations were based on the DFT and implemented in the CASTEP code. A generalized gradient approximation (GGA) with the Per-dew-Burke-Ernzerhof (PBE) method was employed to describe the exchange and correlation energy [22]. The ultrasoft pseudopotentials (USP) with a wave plane energy cutoff of 500 eV was used to ensure convergence. The SCF tolerance was  $1.0 \times 10^{-6}$  eV/atom. Before the surface models construction and surface energy calculations the geometry optimization was first carried out. The optimized  $\beta$ - $\text{Bi}_2\text{O}_3$  cell with 206 atoms was applied to construct the surface models as shown in Fig. 3. In the case of  $\{0\ 0\ 1\}$  surface, a 206 atoms slab was cleaved from the  $\beta$ - $\text{Bi}_2\text{O}_3$  cell, and so the  $\{1\ 0\ 0\}$  and  $\{1\ 1\ 0\}$  surfaces with the same thickness vacuum region. The surface energy ( $E$ ) was computed using the following formula

$$E = \frac{E_s - nE_b}{2A}$$

where  $E_s$  is the energy of the  $\{1\ 1\ 0\}$ ,  $\{1\ 0\ 0\}$  and  $\{0\ 0\ 1\}$  slab,  $E_b$  is the total energy of the  $\beta$ - $\text{Bi}_2\text{O}_3$  bulk per unit cell calculated according to the slab energy,  $A$  is the surface area of the exposed slab surface, and  $n$  is the number of  $\text{Bi}_2\text{O}_3$  bulk contained in the slab [23].

## 3. Results and discussion

Fig. 1a shows a typical TEM image of  $\text{Bi}_2\text{O}_3$  precursor, an individual nanosheet with  $\text{Bi}_2\text{CO}_3\text{O}_2$  impurities and lower crystallinity (according to Fig. 1d(B)). After annealing at 300 °C for 4 h (5 °C/min), the sheet-like morphology was maintained and porous nanostructure (Fig. 1b) was formed which is identified as the tetragonal phase  $\text{Bi}_2\text{O}_3$  ( $\beta$ - $\text{Bi}_2\text{O}_3$ ) with lattice constant  $a = 10.93$ ,  $c = 5.62$  (JCPDS#74-1374) according to the XRD patterns in Fig. 1d(C) and (A). Fig. 1b shows the TEM image of an isolated porous  $\text{Bi}_2\text{O}_3$  single crystalline nanosheet, some quadrilateral holes ranging from 50 to 150 nm are dispersed in the sheet. The high resolution TEM image as shown in Fig. 1c presents a porous nanosheet with crossed lattice fringes corresponding to  $(4\ 4\ 0)$  and  $(4\ 0\ 0)$  crystal facets, respectively. The angle of  $(4\ 4\ 0)$  and  $(4\ 0\ 0)$  facets is estimated to be 88° approaching

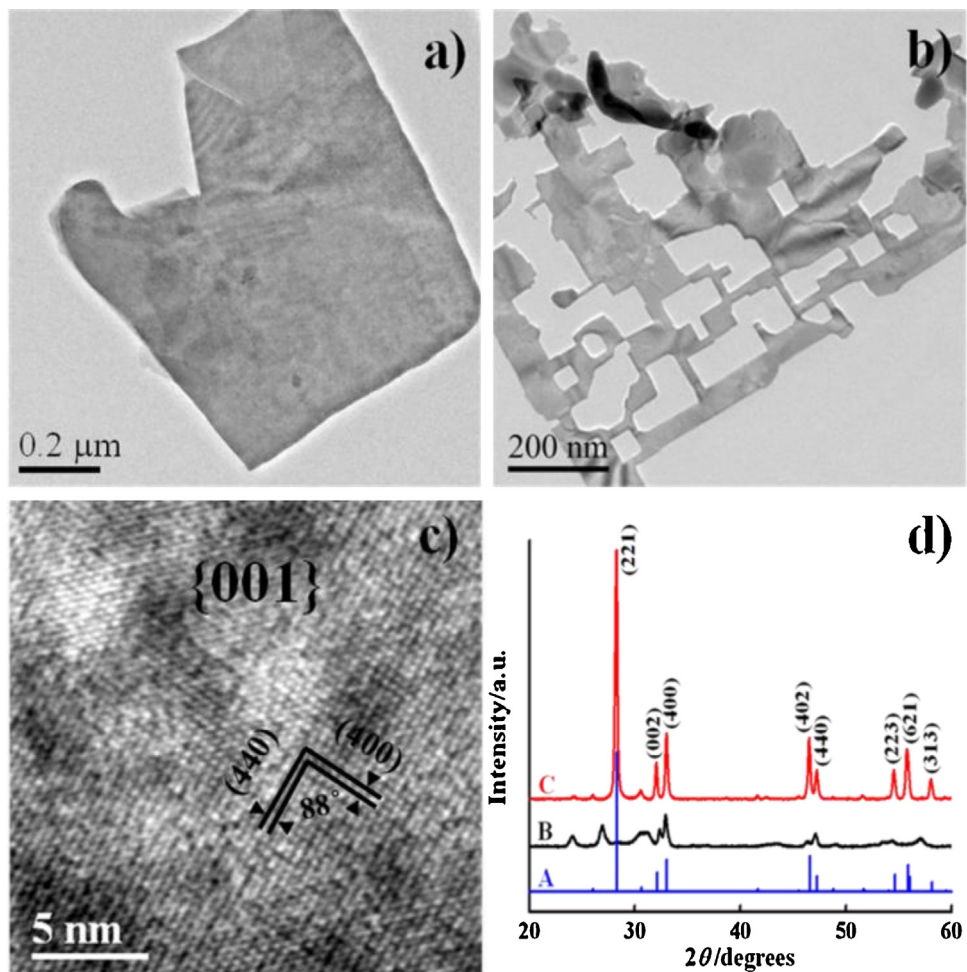


**Fig. 1.** (a) TEM image of  $\text{Bi}_2\text{O}_3$  nanosheet precursor. (b and c) TEM and HRTEM images of single crystalline  $\beta$ - $\text{Bi}_2\text{O}_3$  nanosheet with holes. (d) XRD patterns of porous  $\beta$ - $\text{Bi}_2\text{O}_3$  (A) standard card of JCPDS NO.74-1374, (B) precursor and (C) after calcination ( $300^\circ\text{C}$  for 4 h).

to the actual angle  $90^\circ$ , indicating that the exposed facet is  $\{001\}$  facet.

It was found that the holes in the nanosheets can be divided into two categories on the basis of their shapes, namely irregular and quadrate. Compared with irregular holes, the quadrate holes possess at less one rectangular corner as shown in Fig. 2a and most of the irregular holes are smaller than the quadrate ones due to halfway calcination. More interestingly, for an isolated nanosheet, the edge A and edge B of all the quadrate holes are actually straight and severally parallel to each other. The enlarged TEM image in Fig. 2b clearly shows these features. The details of A and B edges of one quadrate hole are detected by the HRTEM. In Fig. 2c, the lattice spacing is  $0.56\text{ nm}$  and matches well with  $(400)$  facet. As the exposed facet of this nanosheet is  $\{001\}$ , it can be concluded that edge A should correspond to the  $(1-10)$  facet. While the lattice fringe with  $0.78\text{ nm}$  spacing in Fig. 2d parallels to B, edge B should correspond to the  $(110)$  facet. Obviously,  $(110)$  facet is perpendicular to  $(1-10)$  facet and the intersection angles of  $(400)$  facet with  $(110)$  and  $(1-10)$  facets are both  $45^\circ$ . These quadrate holes of  $\beta$ - $\text{Bi}_2\text{O}_3$  are enclosed by the  $\{110\}$  facets. While in general sheet-like  $\text{Bi}_2\text{O}_3$  materials tend to form 3D structures, 2D structure embellished by regular quadrate holes has not been reported. These novel  $\text{Bi}_2\text{O}_3$  nanosheets with quadrate holes should possess promising potential applications in catalysis and energy conversation.

To investigate the formation mechanism of the sheet-like and porous nanostructure, several experiments have been carried out. Fourier transform infrared spectra (FTIR) of the as-prepared

precursor and porous  $\text{Bi}_2\text{O}_3$  nanosheet were employed to compare the differences of the functional groups contained on surfaces as shown in Fig. 3. In Fig. 3a the peak at  $3418\text{ cm}^{-1}$  is a typical stretching vibration of hydroxyl groups. The two intense peaks at  $1531\text{ cm}^{-1}$  and  $1393\text{ cm}^{-1}$  are assigned to the typical asymmetrical and symmetrical stretching vibrations of  $\text{C}=\text{O}$  because of the  $-\text{COOH}$  groups. The double weaker peaks locate at  $1016\text{ cm}^{-1}$  is attributed to the  $\text{C}=\text{O}-\text{C}$  symmetrical stretching vibrations [24]. The  $923\text{ cm}^{-1}$  peak is attributed to the out-of-plane bending of  $\text{C}-\text{OH}$  [25]. The peak at  $846\text{ cm}^{-1}$  is attributed to the  $\text{Bi}-\text{O}-\text{C}$  stretching caused by the  $\text{Bi}_2\text{CO}_3\text{O}_2$  impurities. In Fig. 3b, the peaks at  $1390$ ,  $1262$ ,  $1029$  and  $803\text{ cm}^{-1}$  are all attributed to the  $\text{Bi}-\text{O}$  stretching [26]. The most remarkable differences between the two cures are the peaks at  $3418\text{ cm}^{-1}$  and  $1531$ – $1393\text{ cm}^{-1}$  in Fig. 3a, they disappeared after calcinations. The  $3418\text{ cm}^{-1}$  peak is a typical stretching vibration of hydroxyl groups caused by ethanol, and the two intense peaks at  $1531$  and  $1393\text{ cm}^{-1}$  are assigned to the typical asymmetrical and symmetrical stretching vibrations of  $\text{C}=\text{O}$  in the  $-\text{COOH}$  groups [27]. It indicated that the  $-\text{OH}$  and  $-\text{COOH}$  groups in the as-prepared precursors are important for the formation of the porous nanostructure of  $\text{Bi}_2\text{O}_3$ . When ethanol was substituted with equal amount of n-hexanol, a similar sheet-like  $\text{Bi}_2\text{O}_3$  with quadrate holes and exposed  $\{001\}$  facet was obtained, while the size of an isolate nanosheet reduced. When ethanol was substituted with n-hexane, the size of the nanosheet increased as shown in Fig. 4. It indicates that one of the function of ethanol in this reaction system was to control the sizes of the nanosheets. Though the

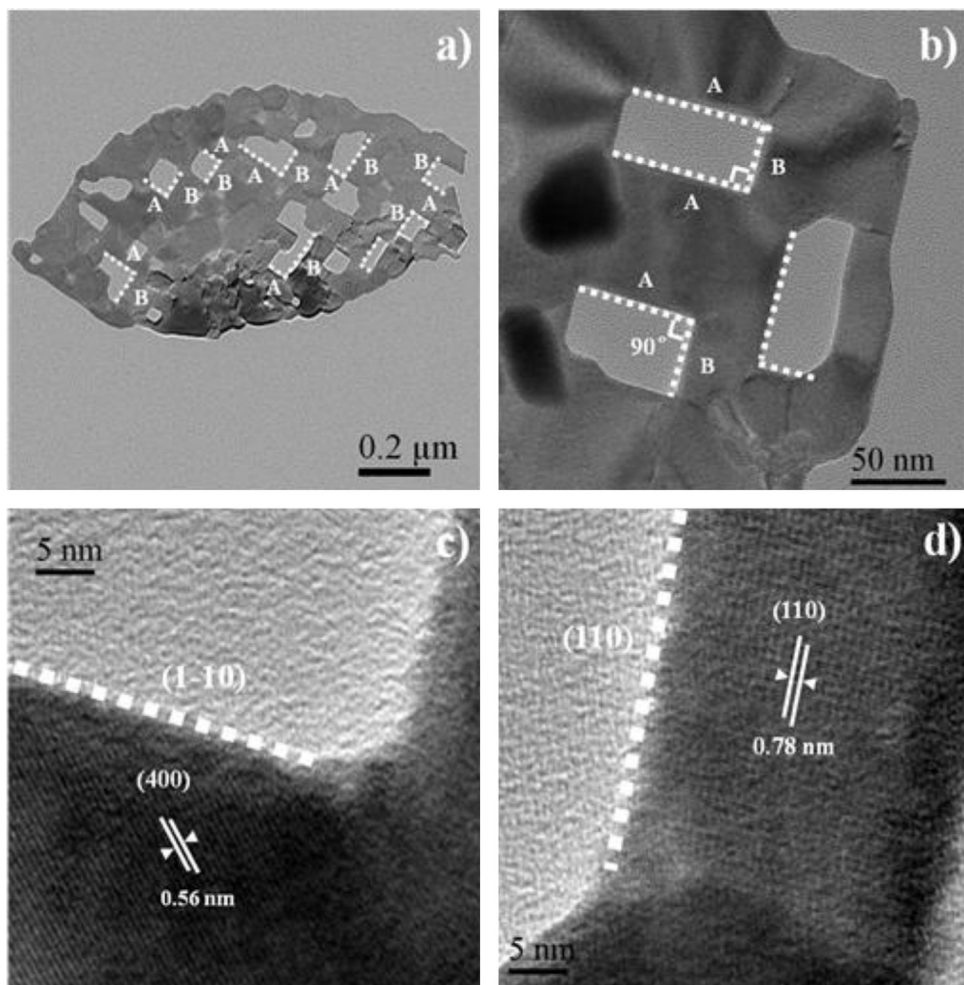


**Fig. 2.** (a and b) TEM images of single crystalline  $\beta$ - $\text{Bi}_2\text{O}_3$  nanosheets with different magnifications. (c and d) HRTEM images of one square hole recorded from its A and B edges alone [001] zone axis.

morphology changes little, the exposed facet of  $\text{Bi}_2\text{O}_3$  is no more the {001} but the {110} facet instead when using the n-hexane, and the relative higher XRD (400) peak of this sample (using n-hexane as the reactant) in Fig. S1 also proves this obvious transformation.

To demonstrate this conclusion and study the function of acetic acid in this system, the amount of ethanol and the reaction time were further varied. When the amount of ethanol was tapered

off, the quantity of holes in an isolated nanosheet decreased concurrently (Fig. 5). The FTIR spectrums of the as-prepared  $\text{Bi}_2\text{O}_3$  precursor in Fig. S2 indicates the variation of the coordination mode between the  $-\text{COOH}$  and  $\text{Bi}^{3+}$  with decreasing the amount of ethanol. For acetic acid and metal ions, there are three coordination modes, unidentate, bidentate and bridging forms (Fig. 6) classified by the vibration frequency difference ( $\Delta\nu$ ) of the  $-\text{COOH}$  double peaks. For monodentate mode,  $\Delta\nu$  is larger than  $200\text{ cm}^{-1}$ , for bidentate mode,  $\Delta\nu$  is less than  $100\text{ cm}^{-1}$  and for bridging mode, it falls in between [28]. On the other hand, the changes of the reaction time have no effect on the final porous sheet-like structure (Fig. 7), while their FTIR spectra alter regularly (Fig. S3). Firstly, the  $\text{Bi}-\text{O}-\text{C}$  peak located at  $846\text{ cm}^{-1}$  and the  $\text{Bi}-\text{O}$  peak located at  $646\text{ cm}^{-1}$  increase until 20 h and then decrease after 30 h, this means the components in the precursors varied along with the reaction time [26,29]. Secondary, the  $\Delta\nu$  values of  $-\text{COOH}$  double peaks at  $1531\text{ cm}^{-1}$  and  $1393\text{ cm}^{-1}$  shift little, nevertheless the relative intensity of the two peaks decrease gradually, implying that the coordination mode between  $\text{Bi}^{3+}$  and  $-\text{COOH}$  also transforms versus reaction time. Therefore, in the present reaction system, the  $-\text{COOH}$  groups of acetic acid determine the formation of the porous  $\text{Bi}_2\text{O}_3$  single crystal nanosheet, and the interaction between  $-\text{COOH}$  and  $\text{Bi}^{3+}$  is regulated by the appropriate amount of ethanol.

The as-prepared  $\beta$ - $\text{Bi}_2\text{O}_3$  single crystal belongs to the tetragonal system which tends to generate sheet structures thermodynamically, and the Bi atoms combine with O atoms in the form of  $[\text{BiO}_6]$

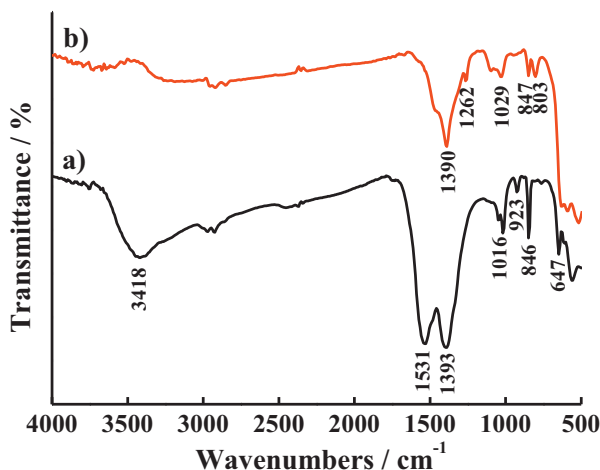


**Fig. 3.** FTIR spectra of (a) the  $\text{Bi}_2\text{O}_3$  precursor for 20 h using 70 mL ethanol and (b) the corresponding porous  $\text{Bi}_2\text{O}_3$  nanosheet.

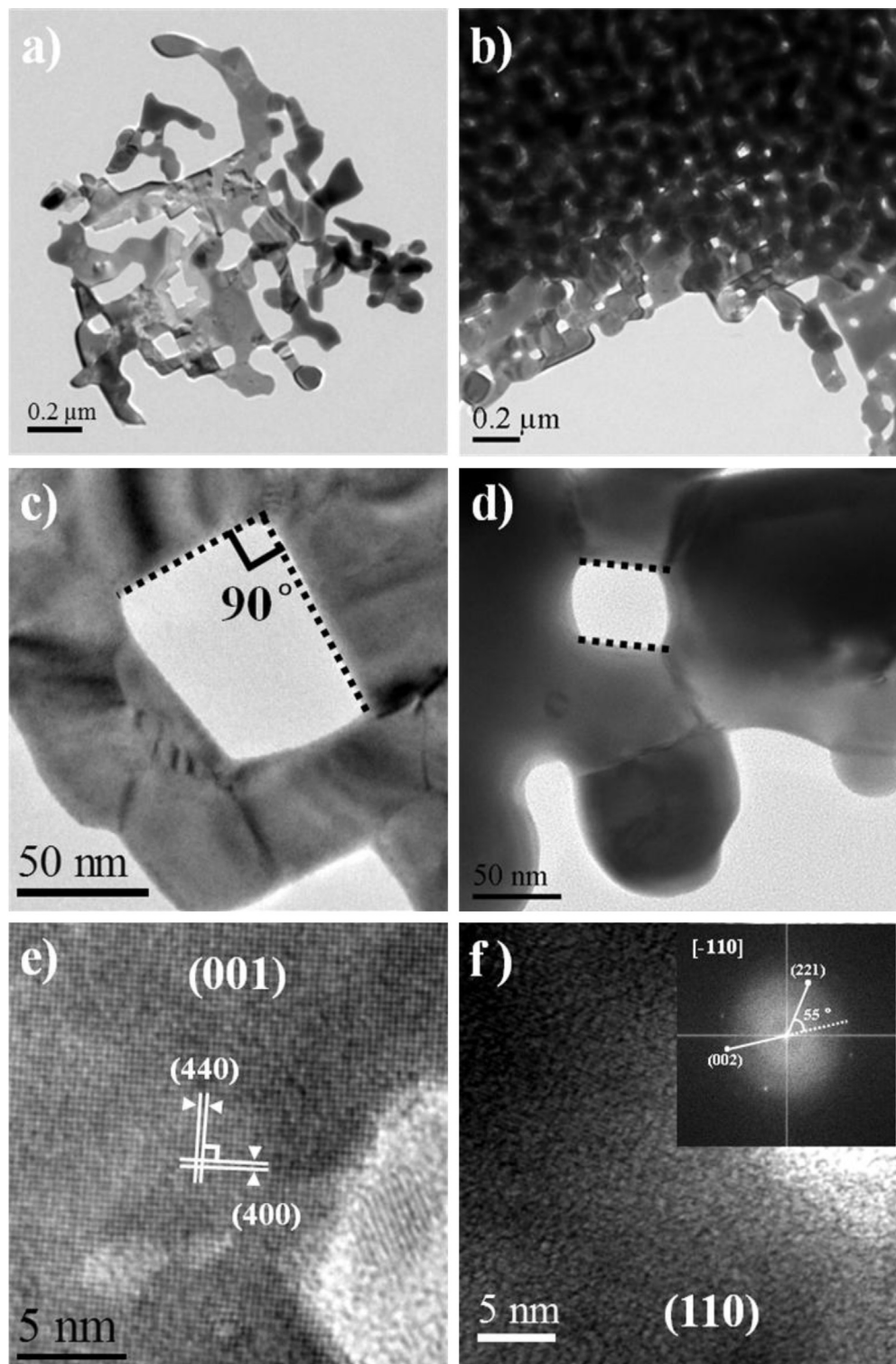


**Fig. 4.** TEM and HRTEM images of  $\text{Bi}_2\text{O}_3$  which synthesized by change ethanol into equal amount of n-hexanol or n-hexane. (a, c, and e) n-hexanol was used, a similar sheet-like  $\text{Bi}_2\text{O}_3$  with quadrate holes and exposed  $\{001\}$  facet was obtained, while the size of the nanosheet reduced. (b, d, and f) n-hexane was used, the size of the nanosheet increased. The inset in (f) is a fast Fourier transform (FFT) pattern, it indicates the exposed facet is  $\{110\}$ .

octahedron. In order to figure out the underlying impetus for forming the  $\{001\}$  facets instead of others, we further investigated the surface energies of  $\beta\text{-Bi}_2\text{O}_3$   $\{100\}$ ,  $\{110\}$  and  $\{001\}$  facets on the basis of the DFT. Fig. 8 shows the surface models of the  $\{110\}$  and  $\{001\}$  surfaces that constructed from a  $\text{Bi}_2\text{O}_3$  cell including 206 atoms, and these surfaces share the same vacuum region thickness. The results showed that the surface energy of  $\{001\}$  facets was

$1.83 \text{ J/m}^2$  which higher than both of  $\{110\}$  ( $1.42 \text{ J/m}^2$ ) and  $\{100\}$  ( $0.98 \text{ J/m}^2$ ) facets, indicating that the  $\{001\}$  facets should be more reactive and unstable than  $\{110\}$  and  $\{100\}$  facets though these surface structures are all consisted of  $[\text{BiO}_6]$  octahedron (Fig. 9). Fig. 9 shows the side and top view ball-and-stick models of  $\beta\text{-Bi}_2\text{O}_3$  that correspond to the  $\{110\}$ ,  $\{100\}$  and  $\{001\}$  facets respectively, the insets in the top views are the  $[\text{BiO}_6]$  octahedron. Though these

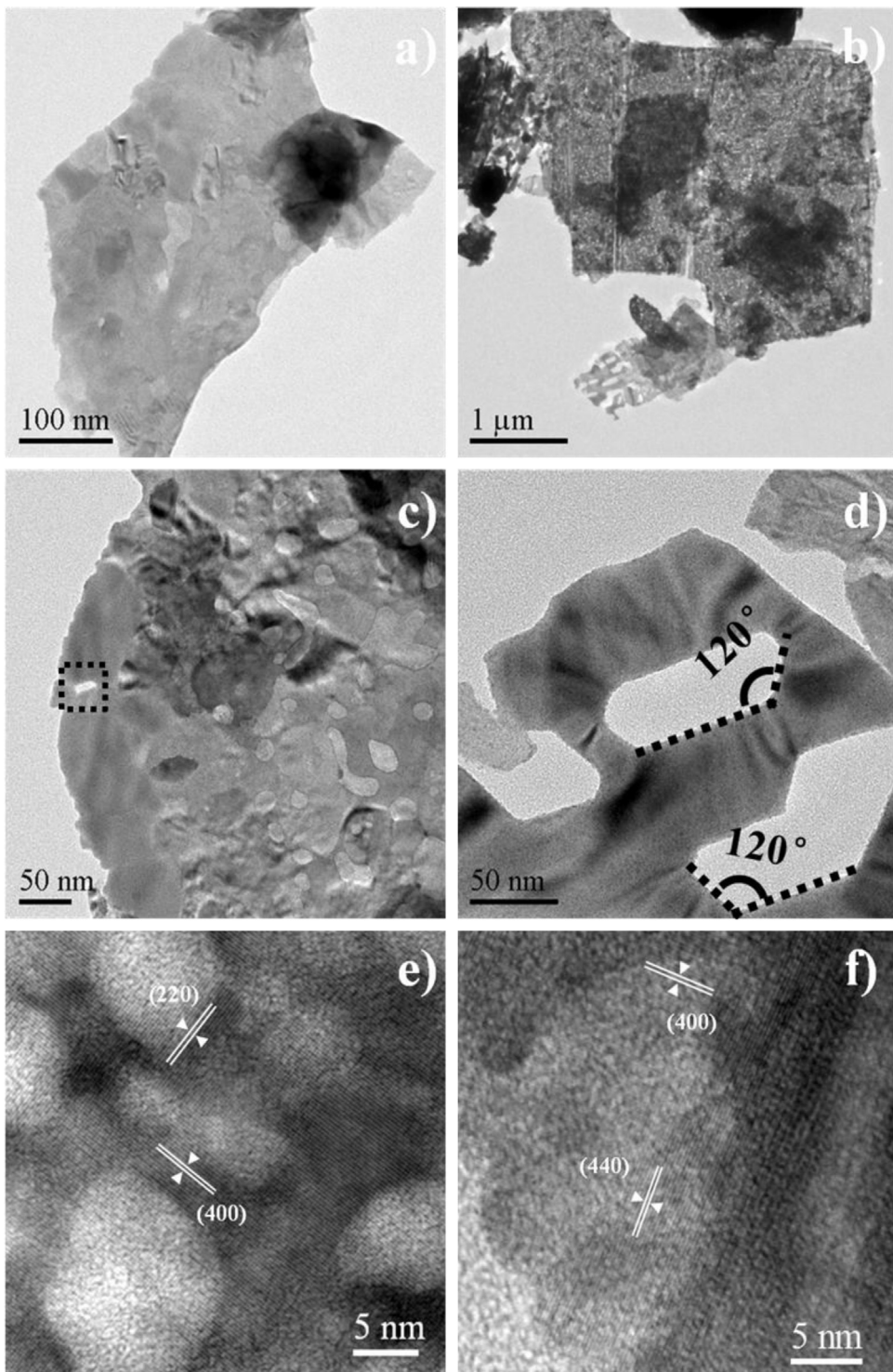


**Fig. 5.** TEM and HRTEM images of  $\text{Bi}_2\text{O}_3$  synthesized in the presence of different amounts of ethanol. (a, c, and e) 10 mL ethanol, the dashed box points out one hole in the  $\text{Bi}_2\text{O}_3$  nanosheet. (b, d, and f) 35 mL ethanol, the as prepared sheet like  $\text{Bi}_2\text{O}_3$  possesses hexagonal holes with  $120^\circ$  angles. Indicating that little ethanol against the formation of porous structure with smaller size, or turn to generate hexagonal holes instead of quadrat with larger size. However, the exposed facets of the two samples are both  $\{001\}$ .

surface structures are all consisted of  $[\text{BiO}_6]$  octahedron, the different arrangements lead to the different surface energies as shown in Fig. 9. In the case of  $\{001\}$  facets, six O atoms equally distribute to the two sides of the Bi atom and the included angle of two surface O atoms is  $108.1^\circ$  which smaller than that of  $\{110\}$  facets ( $116.7^\circ$ ), this means the electron density on the  $\{001\}$  facets is larger than the  $\{110\}$  and  $\{100\}$  facets, and for  $\{100\}$  facets there is only one O atom in the side of the Bi atom. This unique atomic arrangement of

$\{001\}$  facets is in favor of adsorbing alcohol molecules (ethanol and n-hexanol) to reduce its high surface energy and promote the oriented growth and exposed with the  $\{001\}$  facets due to the strong nucleophilic effect between the alcoholic hydroxyls and  $\text{Bi}^{3+}$ . When only a little amount of ethanol was used, acetic acid coordinated with  $\text{Bi}^{3+}$  through a bidentate mode (Fig. 6b). Because of the higher concentration, the reactions of both were very rapid and led to a smaller sheets (Fig. 5a). On the other hand, larger amount of ethanol

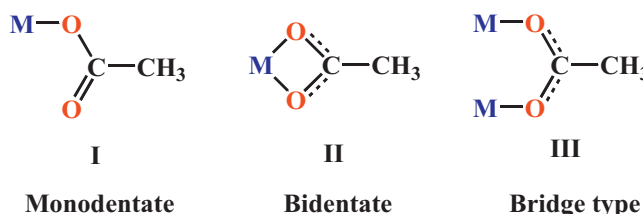


**Fig. 6.** The three coordination modes of acetic acid with metal ions in the solution,  $\Delta[\nu_{\text{as}}(-\text{COOH}) - \nu_{\text{s}}(-\text{COOH})]$  is the basis of classification.

resulted in a bridging mode (Fig. 6c), relative slower reaction rate and bigger sheets (Fig. 5b). n-hexane has a long carbon chain, when adsorbed on the surface of the precursor, the repulsive force among n-hexane molecules should be stronger than that of ethanol, the final sheets thus have smaller sizes (Fig. 4a).

A possible formation mechanism of this novel sheet-like  $\text{Bi}_2\text{O}_3$  single crystal with regular square holes and exposed reactive  $\{0\ 0\ 1\}$  facets was proposed. Fig. 10 exhibits a schematic illustration of the reaction processes of the porous  $\text{Bi}_2\text{O}_3$ . At the first stage (Fig. 10a),  $\text{Bi}^{3+}$ , ethanol and acetic acid molecules (here the two oxygen atoms of the acetic acid are equivalent) coexist in the reaction solution. Then, every two acetic acid molecules simultaneously combine with two  $\text{Bi}^{3+}$  in the bridging mode generating a complex, and the superficially adsorbed alcohol by electrostatic interactions (in Fig. 10,  $\text{R}^1$  refers to ethanol or n-hexanol) contribute to prevent

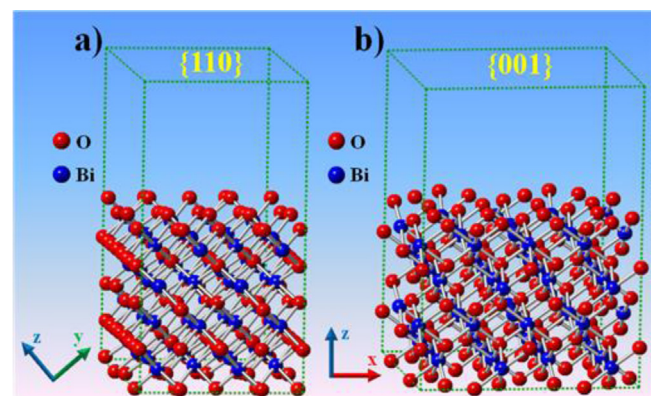


**Fig. 8.** Models for the (a)  $\{1\ 1\ 0\}$  and (b)  $\{0\ 0\ 1\}$  surfaces of  $\beta\text{-Bi}_2\text{O}_3$  on the base of a 206 atoms slab created from the geometry optimized cell.

further longitudinal growth of the complex. This bridging mode features the stronger asymmetrical stretching vibrations than the symmetrical vibrations (see Fig. S3). At the next stage, more acetic acid molecules horizontally combine with the above formed complex forming larger and sheet-like complex (Fig. 1a) in which every  $\text{Bi}^{3+}$  cross connects with four separate acetic acid in the 2D facet forming a network of atoms (Fig. 10c). Instead, this complex feature the stronger symmetrical stretching vibrations than the asymmetrical ones (see Fig. S3). Due to the remaining organics, there are

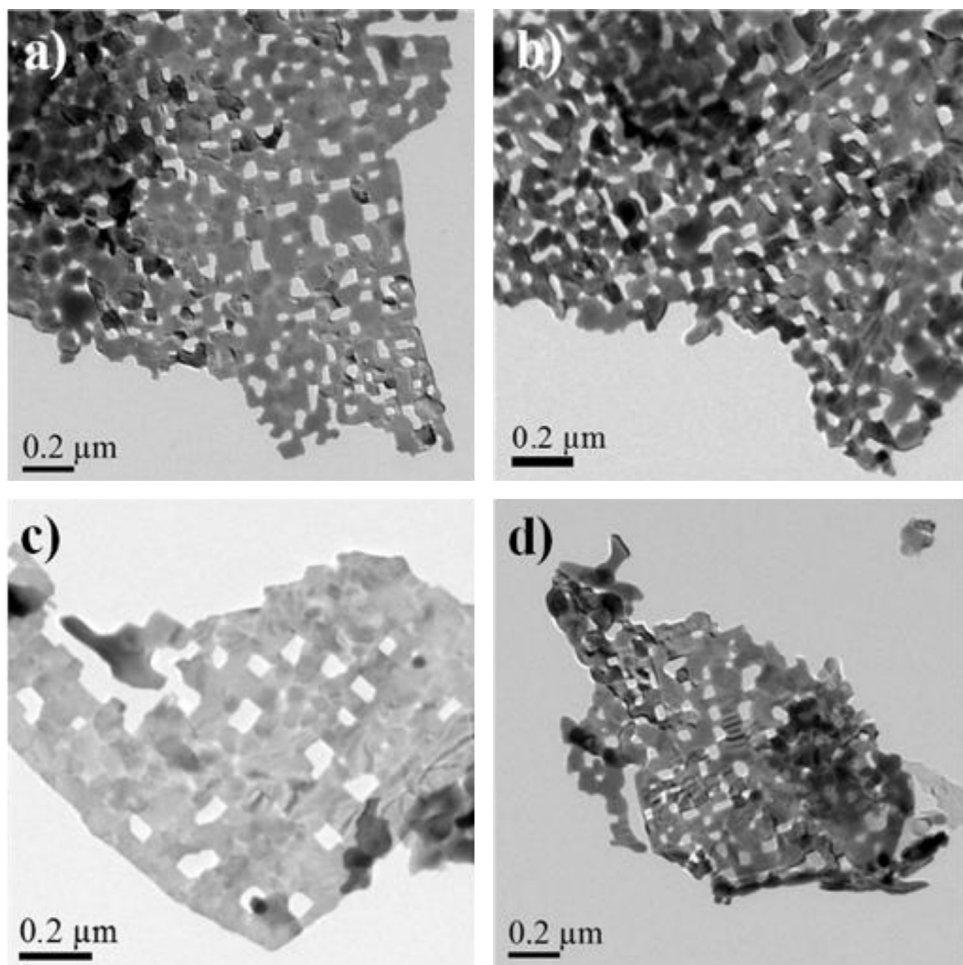


**Fig. 7.** TEM images of porous  $\beta\text{-Bi}_2\text{O}_3$  single crystalline nanosheets for different reaction times (calcination at 300 °C for 4 h) (a) 5 h; (b) 12 h; (c) 20 h; and (d) 30 h.

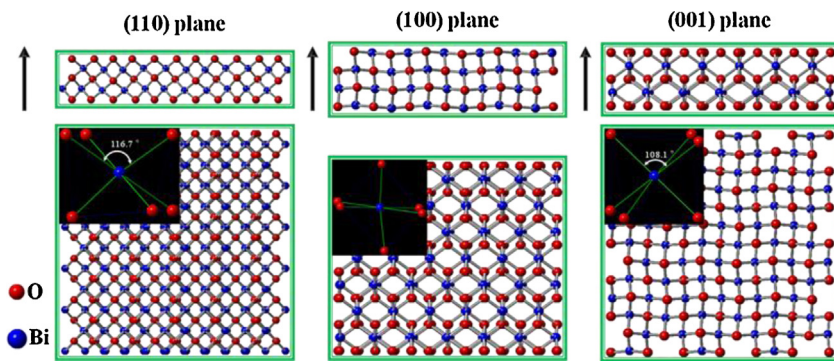


**Fig. 9.** The side and top view ball-and-stick models of  $\beta$ - $\text{Bi}_2\text{O}_3$  that correspond to the  $\{110\}$ ,  $\{100\}$  and  $\{001\}$  facets respectively, the insets in the top views are the  $[\text{BiO}_6]$  octahedron.

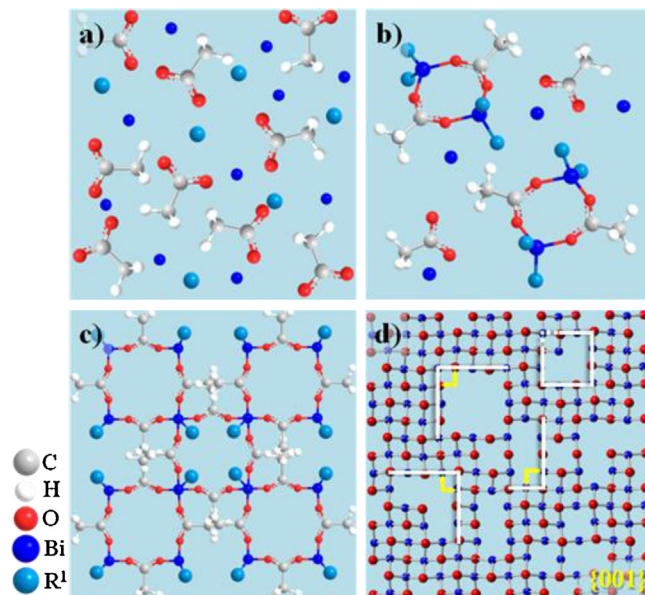


**Fig. 10.** Proposed formation mechanism of the as-prepared single crystalline  $\beta$ - $\text{Bi}_2\text{O}_3$  nanosheets with quadrate holes and exposed  $\{001\}$  facets,  $\text{R}^1$  represents alcohol.

amounts of defects in the finally  $\beta$ - $\text{Bi}_2\text{O}_3$  precursor. On calcination, higher removal rate of the defects than the  $\text{Bi}_2\text{O}_3$  crystallization rate directly lead to the generation of quadrate holes with various sizes in the  $\text{Bi}_2\text{O}_3$  sheets (Fig. 10d) [30,31]. As these defects are uniformly distribute across a single nanosheet, the holes in it are also well scattered. Interestingly, when the precursor was calcined at  $400\text{ }^\circ\text{C}$  for 4 h, porous and sheet-like structures were also acquired, while the micro-sized sheet and huge holes differ from previous structures (Fig. S4).

The as-prepared  $\beta$ - $\text{Bi}_2\text{O}_3$  nanosheets with regular square holes were successfully employed for the degradation of RhB pollutant under irradiation of the simulated sunlight. By introducing the UC element  $\text{Er}^{3+}$  and optimizing the dosage, we have improved the photocatalytic activities of the  $\beta$ - $\text{Bi}_2\text{O}_3$ . As shown in Fig. 11a, the optimal concentration of  $\text{Er}^{3+}$  was 0.8 wt%. Under this conditions, the RhB solution decoloured completely in 30 min, and the corresponding TOC changes in Fig. 11b proved that it was a mineralization process. Both the pure and 0.8 wt%  $\text{Er}^{3+}$  doped  $\beta$ - $\text{Bi}_2\text{O}_3$  exhibited better activities than the sample fabricated in the presence of n-hexane (the exposed facets were  $\{110\}$ ) and commercial  $\text{Bi}_2\text{O}_3$ . The high activity may be attributed to the higher surface energy of  $\{001\}$  facets than  $\{110\}$ . The maximum dosage of  $\text{Er}^{3+}$  was only 1.2 wt%, the doped  $\text{Er}^{3+}$  had little impact on the porous morphology and crystal structure of  $\text{Bi}_2\text{O}_3$  (see Fig. S5). The

absorption peak centered at 654 nm in Fig. 11c is attributed to the electron transition from  $4\text{I}_{15/2}$  to  $4\text{F}_{9/2}$  energy level of  $\text{Er}^{3+}$ , indicating  $\text{Er}^{3+}$  has been doped into the  $\beta$ - $\text{Bi}_2\text{O}_3$  substrate. For pure  $\beta$ - $\text{Bi}_2\text{O}_3$ , the absorbable light is limited to 547 nm (see Fig. 11c), while the dopant  $\text{Er}^{3+}$  in the  $\text{Er}^{3+}$ -doped  $\beta$ - $\text{Bi}_2\text{O}_3$  with right dosage can effectively convert long wavelength light (e.g. IR) to short wavelength light (e.g. visible light) or generate excited electrons with higher energy by sequentially capturing low energy photons (unabsorbable for pure  $\beta$ - $\text{Bi}_2\text{O}_3$ ) as shown in Fig. 11d [32,33]. When these excited electrons relax to the ground state by means of irradiation or energy transformation, the emitted light or transformed energy will make the  $\text{Bi}_2\text{O}_3$  yield more photoinduced  $\text{e}^-$  and  $\text{h}^+$  and enhance the photocatalytic activities. The DRS of 0.8 wt%  $\text{Er}^{3+}$  doped  $\text{Bi}_2\text{O}_3$  also showed the promoted light absorption (marked by blue circle) in Fig. S6.

The approach we developed for porous sheet-like  $\beta$ - $\text{Bi}_2\text{O}_3$  was also employed to synthesis other porous functional materials including porous  $\text{Er}_2\text{O}_3$  and porous  $\text{NiO}$  nanosheets. Fig. S7 shows the TEM images of  $\text{Er}_2\text{O}_3$  and sheet like  $\text{NiO}$  with holes. For  $\text{Er}_2\text{O}_3$ , holes with size of 20–50 nm (marked by white circles) are observed throughout the structure, and for  $\text{NiO}$ , micropores (marked by black circles) are densely distributed in a huge sheet, suggesting the good versatility of this approach in synthesis of other porous materials.

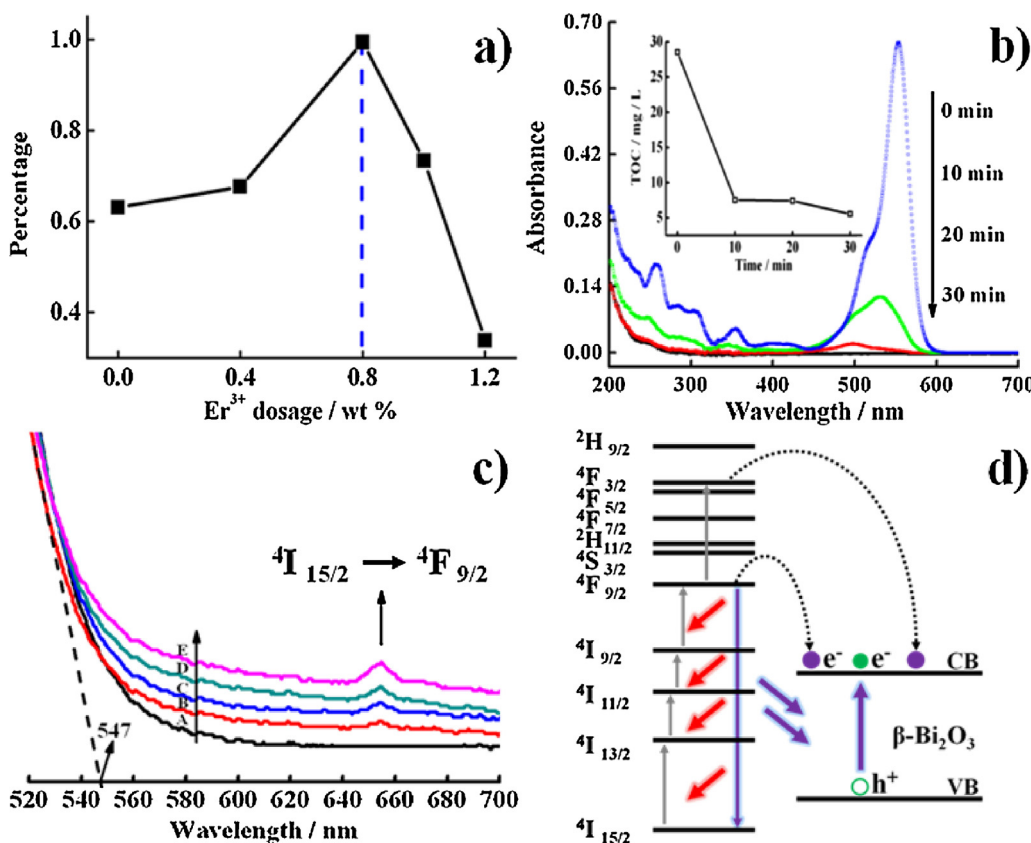


**Fig. 11.** (a) The degradation percentage of RhB versus Er<sup>3+</sup> dosages. (b) Time dependent UV-vis absorbance spectra of RhB solution catalyzed by the 0.8 wt% Er<sup>3+</sup>-doped porous β-Bi<sub>2</sub>O<sub>3</sub> nanosheets under simulated sunlight irradiation, the inset is the change of corresponding TOC values of RhB at different time. (c) The DRS spectra of Er<sup>3+</sup>-doped porous β-Bi<sub>2</sub>O<sub>3</sub> with different dosages of Er<sup>3+</sup> from A to E 0, 0.4, 0.8, 1.0 and 1.2 wt%. (d) A schematic illustration of the energy conversion in the Er<sup>3+</sup>-doped β-Bi<sub>2</sub>O<sub>3</sub> nanosheets.

#### 4. Conclusions

In summary, we have developed a new template-free method to synthesis 2D β-Bi<sub>2</sub>O<sub>3</sub> nanosheets with regular square holes enclosed by the {1 1 0} facets. It is demonstrated that in this system, ethanol acted as a conditioning agent and led to the formation of the high surface energy {0 0 1} facets, the acetic acid contributed to the porous structure by coordinating with Bi<sup>3+</sup> and forming defects in the precursor. The introduction of 0.8 wt% Er<sup>3+</sup> significantly improved the photocatalytic activities of the β-Bi<sub>2</sub>O<sub>3</sub>. The enhanced photocatalytic activity of β-Bi<sub>2</sub>O<sub>3</sub> nanosheets can be attributed to the exposed reactive {0 0 1} facets and the dopant Er<sup>3+</sup> which can transform visible light into ultraviolet light. In addition, this method exhibited good versatility in fabricating porous Er<sub>2</sub>O<sub>3</sub> and NiO.

#### Acknowledgements

The Project was sponsored by the Scientific Research Foundation for the Returned Overseas Chinese Scholars, State Education Ministry. This work was also supported by National Natural Science Foundation of China (20803096, 21073238), the NSF of Hubei Province (Distinguished Young Investigator Grant 2010CDA082), and National Basic Research Program of China (Grant No. 2011CB211704).

#### Appendix A. Supplementary data

Supplementary data associated with this article can be found, in the online version, at <http://dx.doi.org/10.1016/j.apcatb.2013.04.009>.

#### References

- [1] J. Zhang, Q. Xu, Z.C. Feng, M.J. Li, C. Li, *Angewandte Chemie International Edition* 47 (2008) 1766.
- [2] Z.R. Tian, J.A. Voigt, J. Liu, B. Mckenzie, M.J. Mcdermott, M.A. Rodriguez, H. Konishi, H.F. Xu, *Nature Materials* 2 (2003) 821.
- [3] L. Etgar, W. Zhang, S. Gabriel, S.G. Hickey, M.K. Nazeeruddin, A. Eychmüller, B. Liu, M. Grätzel, *Advanced Materials* 24 (2012) 2202.
- [4] C.Y. Chao, Z.H. Ren, Y.H. Zhu, Z. Xiao, Z.Y. Liu, G. Xu, J.Q. Mai, X. Li, G. Shen, G.R. Han, *Angewandte Chemie International Edition* 51 (2012) 9283.
- [5] B. Reeja-Jayan, E. De la Rosa, S. Sepulveda-Guzman, R.A. Rodriguez, M. Jose Yacaman, *Journal of Physical Chemistry C* 112 (2008) 240.
- [6] Y. Zhang, A.H. Yuwono, J. Wang, J. Li, *Journal of Physical Chemistry C* 113 (2009) 21406.
- [7] H.G. Yang, C.H. Sun, S.Z. Qiao, J. Zou, G. Liu, S.C. Smith, H.M. Cheng, G.Q. Lu, *Nature* 453 (2008) 638.
- [8] J. Jiang, K. Zhao, X.Y. Xiao, L.Z. Zhang, *Journal of the American Chemical Society* 134 (2012) 4473.
- [9] Y.P. Bi, S.X. Ouyang, N. Umezawa, J.Y. Cao, J.H. Ye, *Journal of the American Chemical Society* 133 (2011) 6490.
- [10] X.W. Xie, Y. Li, Z.Q. Liu, M. Haruta, W.J. Shen, *Nature* 458 (2009) 746.
- [11] F. Wang, C.H. Li, L.D. Sun, C.H. Xu, J.F. Wang, J.C. Yu, C.H. Yan, *Angewandte Chemie International Edition* 51 (2012) 4872.
- [12] H. Zhang, H. Wang, Y. Xu, S.F. Zhuo, Y.F. Yu, B. Zhang, *Angewandte Chemie International Edition* 51 (2012) 1459.
- [13] J. Zhang, F.J. Shi, J. Lin, D.F. Chen, J.M. Gao, Z.X. Huang, X.X. Ding, C.C. Tang, *Chemistry of Materials* 20 (2008) 2937.
- [14] C. Zhang, Y.F. Zhu, *Chemistry of Materials* 17 (2005) 3537.
- [15] J.C. Hu, X.L. Zhou, T.F. Zhou, X.T. Li, W.G. Cheng, *Journal of South-Central University for Nationalities (Nature Sciences Edition)* 1 (2012) 8.
- [16] J.Q. Yu, A. Kudo, *Advanced Functional Materials* 16 (2006) 2163.
- [17] Y. Qiu, D. Liu, J. Yang, S. Yang, *Advanced Materials* 18 (2006) 2604.
- [18] Y.D. Shen, Y.W. Li, W.M. Li, J.Z. Zhang, Z.G. Hu, J.H. Chu, *Journal of Physical Chemistry C* 116 (2012) 3449.
- [19] H. Zhang, P. Wu, Y. Li, L.F. Liao, Z. Fang, X.H. Zhong, *ChemCatChem* 2 (2010) 1115.
- [20] L. Zhou, W.Z. Wang, H.L. Xu, S.M. Sun, M. Shang, *Chemistry: A European Journal* 15 (2009) 1776.

- [21] K. Brezesinski, R. Ostermann, P. Hartmann, J. Perlich, T. Brezesinski, *Chemistry of Materials* 22 (2010) 3079.
- [22] C.J. Duan, X.J. Wang, W.M. Otten, A.C.A. Delsing, J.T. Zhao, H.T. Hintzen, *Chemistry of Materials* 20 (2008) 1597.
- [23] Y. Wang, J. Chen, P. Wang, L. Chen, Y.B. Chen, L.M. Wu, *Journal of Physical Chemistry C* 113 (2009) 16009.
- [24] Z.Y. Zhou, D.J. Chen, H. Li, Q. Wang, S.G. Sun, *Journal of Physical Chemistry C* 112 (2008) 19012.
- [25] F.W. Pi, F. Kaneko, M. Iwahashi, M. Suzuki, Y. Ozaki, *Journal of Physical Chemistry B* 115 (2011) 6289.
- [26] L. Liu, J. Jiang, S.M. Jin, Z.M. Xia, M.T. Tang, *CrystEngComm* 13 (2011) 2529.
- [27] F. Jalilehvand, V. Mah, B.O. Leung, J. Mink, G.M. Bernard, L. Hajba, *Inorganic Chemistry* 48 (2009) 4219.
- [28] V. Robert, G. Lemercier, *Journal of the American Chemical Society* 128 (2006) 1183.
- [29] D.P. Dutta, M. Roy, A.K. Tyagi, *Dalton Transactions* 41 (2012) 10238.
- [30] F. Li, Y. Ding, P.X. Gao, X.Q. Xin, Z.L. Wang, *Angewandte Chemie International Edition* 43 (2004) 5238.
- [31] J.C. Hu, K.K. Zhu, L.F. Chen, H.J. Yang, Z. Li, A. Suchopar, R. Richards, *Advanced Materials* 20 (2008) 267.
- [32] M. Haase, H. Schäfer, *Angewandte Chemie International Edition* 50 (2011) 5808.
- [33] W. Wei, T.C. He, X. Teng, S.X. Wu, L. Ma, H. Zhang, J. Ma, Y.H. Yang, H.Y. Chen, Y. Han, H.D. Sun, L. Huang, *Small* 8 (2012) 2271.